



ELSEVIER

Contents lists available at [ScienceDirect](https://www.sciencedirect.com)

Journal of Building Engineering

journal homepage: www.elsevier.com/locate/job

Mechanical performance and microstructure evolution of MgO-doped high volume GGBFS-based engineered cementitious composites at room and elevated temperatures

S. Rawat ^a, Jitraporn Vongsvivut ^b, Lihai Zhang ^c, Y.X. Zhang ^{a,*}

^a Centre for Advanced Manufacturing Technology, School of Engineering, Design and Built Environment, Western Sydney University, NSW, 2751, Australia

^b Infrared Microspectroscopy (IRM) Beamline, ANSTO-Australian Synchrotron, Clayton, VIC, 3168, Australia

^c School of Infrastructure Engineering, The University of Melbourne, VIC, 3010, Australia

ARTICLE INFO

Keywords:

Engineered cementitious composite

Elevated temperature

MgO

Microstructure

ABSTRACT

This paper presents a comprehensive study on the effect of MgO on the mechanical performance of ternary or quaternary blended engineered cementitious composites (ECC) primarily composed of cement, silica fume, and a high volume of ground granulated blast furnace slag (GGBFS) at both room and elevated temperatures. The study evaluates the mechanical performance with varying dosages of MgO and GGBFS, focusing on compressive strength, tensile strength, and residual compressive strength, along with strength variation and microstructural evolution analysis at different temperatures. Microstructural characterization was performed using scanning electron microscopy, X-ray diffraction, and differential scanning calorimetry techniques, with further analysis of the interfacial transition zone (ITZ) conducted using synchrotron Fourier-transform infrared microspectroscopy. Test results indicated that 10–20 % MgO can be utilized in combination with GGBFS to develop high-strength and high-ductility ECC even at total cement replacement level as high as 80 %. Furthermore, elevated temperature analysis revealed the beneficial effect of MgO addition, particularly due to its hydration-retarding properties which led to accelerated strength development at later stages and resulted in higher residual strength. A compressive strength retention of over 45 % was observed for mixes containing 60 % GGBFS and 10 % MgO. While silica fume addition was found beneficial in terms of enhanced hydration until 200 °C, it led to spalling at high temperatures despite higher dosage of GGBFS. Analysis of the ITZ in the MgO-based matrix further showed the formation of a densely packed calcium silicate hydrate (C-S-H) and calcite around brucite, indicating a strong interface. Magnesium silicate hydrate (M-S-H) was also observed through X-ray diffraction analysis and was found in the matrix till 400 °C, possibly contributing to strength development and higher retention.

1. Introduction

Engineered cementitious composites (ECC) have gained widespread recognition for their exceptional tensile strain capacity and controlled crack behaviour [1,2]. Their intrinsically tight crack width further contributes to enhancing durability, leading to greater

* Corresponding author.

E-mail address: Sarah.Zhang@westernsydney.edu.au (Y.X. Zhang).

<https://doi.org/10.1016/j.job.2024.111437>

Received 13 October 2024; Received in revised form 20 November 2024; Accepted 27 November 2024

Available online 28 November 2024

2352-7102/© 2024 The Authors.

Published by Elsevier Ltd.

This is an open access article under the CC BY license

(<http://creativecommons.org/licenses/by/4.0/>).

resistance against alkaline environment, freeze-thaw attack, chloride and sulphate attack, and other common durability issues encountered in structures [3–5]. However, this performance is achieved by eliminating coarse aggregates resulting in excessive use of cement, sometimes even exceeding 1000 kg per cubic meter, which can result in significant carbon emissions [6]. To address this issue, researchers have explored developing more environmentally friendly ECC by substituting cement with supplementary cementitious materials (SCM) such as fly ash, ground granulated blast furnace slag (GGBFS), silica fume, rice husk ash and calcined clay [7–14]. Mortar containing these SCMs especially GGBFS (in both small and high volumes) has been shown to provide comparable or improved long-term strength compared to OPC-based mortar [15,16].

Among other emerging alternative binders, reactive MgO has gained significant attention both as separate binder system and as an additive due to its lower production temperature and strength gain potential by reacting with atmospheric CO₂ [17–20]. Recent studies have also demonstrated its utility as an expansive agent for controlling shrinkage [21]. The MgO concrete dam technique, which utilizes the delayed expansion properties of MgO, has been successfully used in dam construction in China for over 50 years [22]. Moreover, MgO can also improve the strength of cement-based materials if present in an optimal amount. The hydration products, including brucite, hydrotalcite-like phases, calcium silicate hydrate, and portlandite, collectively contribute to densifying the matrix [18]. When combined with SCMs, the strength improvement stems from the formation of additional C–S–H through the reaction of SCMs with Ca(OH)₂, as well as the formation of M–S–H through the reaction with MgO, which strengthens the bond within the cement matrix [22]. However, the role of MgO within an ECC system and an optimum amount in terms of optimal performance remains unclear due to very limited studies in this area.

Recently, Wu et al. [18] studied the mechanical performance of ECC with fly ash as the main SCM and MgO as an additional binder. They reported a significant decrease in compressive strength from 52.8 MPa to 34.4 MPa with the addition of 10 % by weight MgO. However, they also observed a significant reduction in permeability and porosity of the composite and an improvement in the tensile strength and ultimate tensile strength with the addition of MgO. Gonçalves et al. [21] also observed a reduction in compression and flexural strength with increase in dosage of MgO in ordinary Portland cement (OPC) based matrix. Wu et al. [23] further corroborated that addition of MgO may lead to improved tensile strength and ultimate tensile strain, however, the first cracking strength may decrease. Sherir et al. [24] also highlighted the excellent self-healing properties of ECC with MgO, reporting that MgO contributes to a denser matrix and improved durability. Their findings indicated that specimens with up to 30 % MgO content showed minimal expansion in water and autoclave linear expansion tests.

Despite the excellent performance of MgO, the present knowledge is limited to its role as an expansive agent in enhancing durability, and there is insufficient understanding of how MgO affects the mechanical properties of ECC. Additionally, the compatibility of MgO with ECC formulations, especially those with high volumes of SCMs, remains uncertain. This knowledge is crucial given the potential applications of ECC in high-rise buildings and retrofit applications. While it typically experiences high strength loss beyond 600 °C [25–28], the inclusion of MgO may intensify this effect, especially considering the decomposition of the MgO hydration phases before 450 °C. Therefore, a comprehensive understanding of the behaviour of MgO-doped ECC at both ambient and elevated temperatures is essential for its wider practical application.

This study investigates the utilization of MgO as a doping agent in high-volume GGBFS-based ECC, aiming to systematically assess its effects on mechanical performance at both room temperature and elevated temperatures. In order to enhance environmental friendliness, cement is substituted by 70–80 % SCM comprising varying proportions of GGBFS and MgO, along with silica fume (SF). A detailed investigation is carried out to understand the effect of various constituents on compressive strength and tensile stress-strain behaviour of this green composite at room temperature. Moreover, the compressive strength of the materials at elevated temperature has also been analysed after exposure to temperatures ranging from 200 to 800 °C. Advanced microstructural analysis techniques such as scanning electron microscopy (SEM), differential scanning calorimetry (DSC), and X-ray diffraction (XRD) analysis are further employed to analyse the hydration stages of MgO doped ECC at different temperature range. Moreover, synchrotron attenuated total reflectance Fourier transform infrared (ATR-FTIR) microspectroscopy has also been utilized to assess the chemical change at interfaces change from room to elevated temperatures. The study provides further recommendation and justification for effectively integrating MgO into ECC to achieve optimal performance under both room and elevated temperature conditions.

2. Materials and methods

2.1. Mix constituents and design

The binders used in the current study included cement (CaO = 63.6 %, SiO₂ = 21.2 %), GGBFS (CaO = 51.5 %, SiO₂ = 28.9 %, Al₂O₃ = 11.4 %, >95 % passing through 45- μ m), silica fume (SiO₂ ~ 95 %) and MgO powder. The general-purpose cement and GGBFS were sourced from Independent Cement, Australia and conformed to Australian Standard AS 3972 and AS3582.2, respectively. The MgO powder, branded as EMAG45, was supplied by QMag, Queensland, Australia. It had a purity greater than 95 % (MgO + CaO = 98.02 %), with over 98 % passing through a 45- μ m sieve, and its chemical reactivity was 73 % assessed as per WB/T 1019 [29]. Oven-dried local Sydney sand, passing through a 500- μ m sieve, was used as the fine aggregate. The use of oven-dried local Sydney sand as a substitute for traditional silica sand was aimed to balance cost-effectiveness and structural suitability. ADVA 650 supplied by GCP technologies was used as the high range water reducer (HRWR) to ensure a consistent workability is achieved. The study utilized a hybrid combination of polyethylene (PE) fibres (12 mm long, 24 μ m dia.) and basalt fibres (12 mm long, 13 μ m dia.). Previous studies have shown that hybrid fibre combination effectively prevents spalling and maintains higher residual strength without compromising room temperature compressive and tensile performance [25]. The fibre proportion was kept fixed to 1.25 % PE + 0.75 % basalt fibre as recommended by Ahmad et al. [30] to obtain optimum room temperature performance. Table 1 lists the constituent proportions of the

Table 1
Mix proportions adopted in the present study.

Mix ID	Binder				Sand	Water	HRWR
	OPC	GGBFS	MgO	SF			
PC30-BFS70	1	2.33	0.00	0.00	1.21	0.83	0.01
PC20-BFS80	1	4.00	0.00	0.00	1.82	1.25	0.02
PC20-BFS70-SF10	1	3.50	0.00	0.50	1.82	1.25	0.02
PC30-BFS60-M10	1	2.00	0.33	0.00	1.21	0.83	0.01
PC30-BFS50-M20	1	1.67	0.67	0.00	1.21	0.83	0.02
PC20-BFS50-M30	1	2.50	1.50	0.00	1.82	1.25	0.02
PC20-BFS60-M10-SF10	1	3.00	0.50	0.50	1.82	1.25	0.02
PC20-BFS50-M20-SF10	1	2.50	1.00	0.50	1.82	1.25	0.03

Note: All quantities are expressed as weight proportion of the cement content. Fibre volume (1.25 % PE and 0.75 % Basalt fibre) was kept constant for each mix.

8 mixes adopted in the current study.

Water to binder content and sand to binder content were kept constant to 0.25 and 0.36, respectively. Mix PC30-BFS70 contained 30 % cement and 70 % GGBFS. The total binder content (OPC + SCM) and other proportions of the mix such as sand-binder and water-binder content were adopted from Rawat et al. [12,31] as this composition showed superior compressive and tensile performance both at room temperature and elevated temperatures. Mix PC30-BFS70 was then modified to incorporate a higher amount of GGBFS, aiming to enhance the sustainability and assess its fire resistance. To analyse the effect of high replacement ratio of GGBFS, the GGBFS replacement amount was further increased to 80 % in mix PC20-BFS80. Additionally, this mix was doped with 10 % silica fume in mix PC20-BFS70-SF10 to distinctly analyse the effect of silica fume. MgO was also added to mix PC30-BFS70 at three replacement ratios (10 %, 20 %, and 30 %) to examine the effect of MgO addition on mechanical properties at room temperature and elevated temperatures. The last two mixes PC20-BFS60-M10-SF10 and PC20-BFS50-M20-SF10 also contained silica fume as doping agent at 10 % replacement ratio. This was done to investigate the effects of a quaternary blend of cement, GGBFS, MgO, and silica fume, and to determine if the addition of silica fume could further enhance the mechanical performance of MgO-doped ECC mixes.

2.2. Specimen preparation

A 40-L planetary mixer was used to prepare the mixes. The mixing started with the dry mixing of all binder materials and sand for approximately 3 min. Half of the calculated HRWR and water (as a solution) were then added into the mix and the mixing continued for another 2–3 min until lumps began to form. Subsequently, the remaining HRWR-water solution was added, and the mixing continued for an additional 2 min. At this stage, homogenous mixture was expected with a flowability of around 200–210 mm measured through the flow table test. If the flowability was found insufficient, additional HRWR was added in increments of 0.5 L/m³ and mixed for 1–2 min. Once the desired flowability was achieved, PE and basalt fibres were added into the mix and the mixing continued for another 5 min. The fresh mix was then poured into the stainless-steel moulds for compression and tension tests. 50 mm cube specimens were casted for compressive and residual compressive strength tests. In addition, dog bone specimens were utilized for assessing tensile stress-strain behaviour. The specimens were demoulded 24 h after casting and stored in the temperature-controlled water tank maintained at 20 ± 2 °C for 28 days. Following the curing period, the specimens were removed from the water tank and stored in environmental chamber at 25 ± 2 °C and 65 ± 5 % relative humidity until the testing phase.

2.3. Testing methods

2.3.1. Elevated temperature exposure

Cubic specimens were heated in the furnace at target temperatures of 200, 400, 600, and 800 °C. The heating rate was maintained at 2 °C/min to effectively study material properties. A slow heating rate was adopted to minimize the damage due to thermal gradient damage so that the behaviour of each matrix could be accurately assessed. Despite this, temperature variations may still occur between specimen surface and cores [32,33]. Therefore, a 2-h dwell period at target temperature was further adopted to ensure uniformity across mixes. After this period, the specimens were naturally cooled inside the furnace [34].

2.3.2. Mechanical performance tests

Following heat treatment, the cubic specimens were tested under compression at a loading rate of 0.1 mm/min using a 5000 kN MTS compressive testing machine. Concurrently, non-heated cubic and dogbone specimens were also tested to assess their compressive and tensile strength, respectively, under room temperature conditions at the same age. For tensile tests, dog-bone specimens with size 340 mm (length) × 50 mm (width) × 13 mm (thickness) and a reduced width of 30 mm with 60 mm gauge length was used. The test was conducted at a loading rate of 0.1 mm/min on Instron 5985 machine with 250 kN capacity. More details about this test setup can be found in Rawat et al. [35]. Three samples were tested for each set and at each temperature range to obtain a representative result.

2.3.3. SEM analysis

A detailed characterization study was conducted to elaborate on phase development and changes in MgO-doped ECC at room and

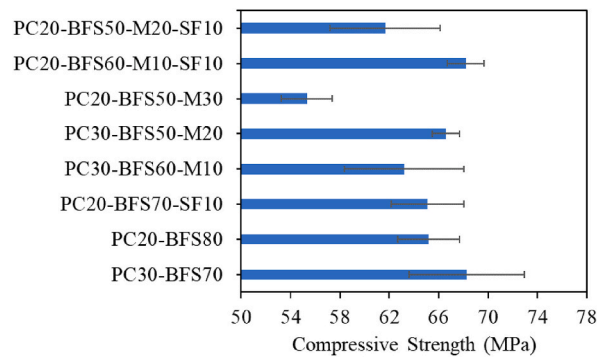


Fig. 1. Compressive strength of the mixes considered in the study.

elevated temperatures. Phenom XL scanning electron microscope was used for the SEM analysis. Samples extracted from the tested cubic specimens were first carbon-coated using a Leica EM SCD005 sputter coater and the coated samples were then analysed in the SEM at 15 kV and 1 Pa chamber pressure.

2.3.4. XRD and DSC analysis

XRD and DSC analyses were conducted on powdered samples extracted from the tested cubic specimens, ground to less than 300 μm . Diffraction patterns were collected using a Bruker D8 Advance powder diffractometer with a LynxEye XE-T position-sensitive detector at 40 kV and 40 mA. A scan range of 5–80° 2 θ , with a step size of 0.02° and counting time of 2.5 s per step, was used. Phases were identified using Bruker Eva v6 software. DSC analysis was performed using a Netzsch STA 449F5 to study the thermal decomposition process and mass loss at different temperatures. Each sample, approximately 20 \pm 0.5 mg, was heated from 40 °C to 800 °C at a rate of 10 °C/min under Argon flow. Both XRD and DSC data were qualitatively analysed to distinguish between different peaks and to understand the variation in compressive strength observed at room and elevated temperatures.

2.3.5. Synchrotron ATR-FTIR microspectroscopy

To understand the MgO interface with the surrounding matrix and corresponding damage at elevated temperatures, synchrotron ATR-FTIR microspectroscopic measurements were performed on Infrared Microspectroscopy (IRM) beamline at ANSTO – Australian Synchrotron (Victoria, Australia). The sample extracted from the tested cube specimens was first polished and thereafter the interface between MgO and the cementitious matrix was observed and imaged, using an in-house developed macro-ATR-FTIR device equipped with a 100- μm -diameter facet germanium (Ge) ATR crystal ($n_{\text{Ge}} = 4.0$), and a 20 \times IR objective (NA = 0.60; Bruker Optik GmbH, Ettlingen, Germany) [36]. High resolution synchrotron ATR-FTIR spectral maps was acquired on interface areas, using a projected aperture size of 3.1 μm and 1 μm step interval between measurement points, with 256 and 16 co-added scans used for background (air) and sample measurements, respectively. All the synchrotron ATR-FTIR spectra were recorded within a spectral range of 3900–750 cm^{-1} using 4- cm^{-1} spectral resolution. Blackman-Harris 3-Term apodization, Mertz phase correction, and zero-filling factor of 2 were set as default acquisition parameters using OPUS 8.0 software suite (Bruker). Atmospheric compensation was subsequently applied on every synchrotron ATR-FTIR spectral map to remove the presence of atmospheric water vapor and carbon dioxide from the spectra, using OPUS 8.0 software suite.

After that, a multivariate pattern recognition method based on hierarchical cluster analysis (HCA) was performed on the corrected spectral maps using CytoSpec v. 2.00.07 (Cytospec Inc., Boston, MA, USA). Here, the spectra embedded in each corrected spectral map were initially pre-processed using noise reduction, 2nd derivatization with 17-point Savitzky-Golay algorithms, and vector normalisation. HCA was then applied using Ward's algorithm and 7 clusters, based on three spectral ranges (3750-3650 cm^{-1} , 2990-2790 cm^{-1} and 1800-920 cm^{-1}) that contain major characteristic absorption bands associated to the key compounds used in these ECC samples.

3. Mechanical performance at room temperature

3.1. Compressive strength

Fig. 1 shows the compressive strength variation of all mixes with change in the binder type and dosage. Notably, even at exceptionally high cement replacement rates (70–80 %), the compressive strength of all mixes exceeded 55 MPa, classifying them as high strength according to ACI 316 classification [37]. The adopted mixes showed compressive strength in range of 55–68 MPa and the highest compressive strength was observed for mix with 30 % OPC and 70 % GGBFS. At higher levels of MgO replacement, a reduction in strength was noted. This is mainly because MgO does not participate in forming primary hydration products and may remain unhydrated when present in larger quantity. This observation further validates that the incorporation of MgO as a substitute for cement or GGBFS may not necessarily promote strength.

A further comparison can be made using Fig. 2. As seen in Fig. 2(a), replacing MgO with GGBFS initially decreased the strength,

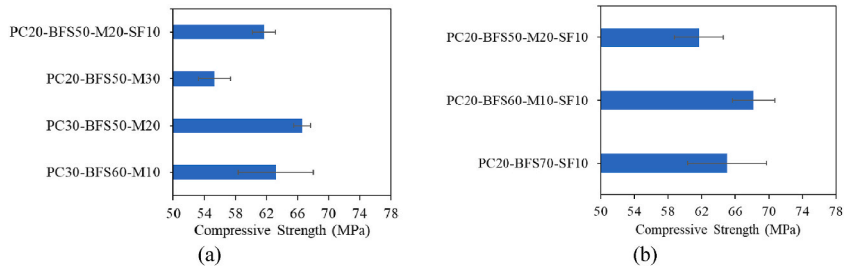


Fig. 2. Effect of MgO addition on the compressive strength.

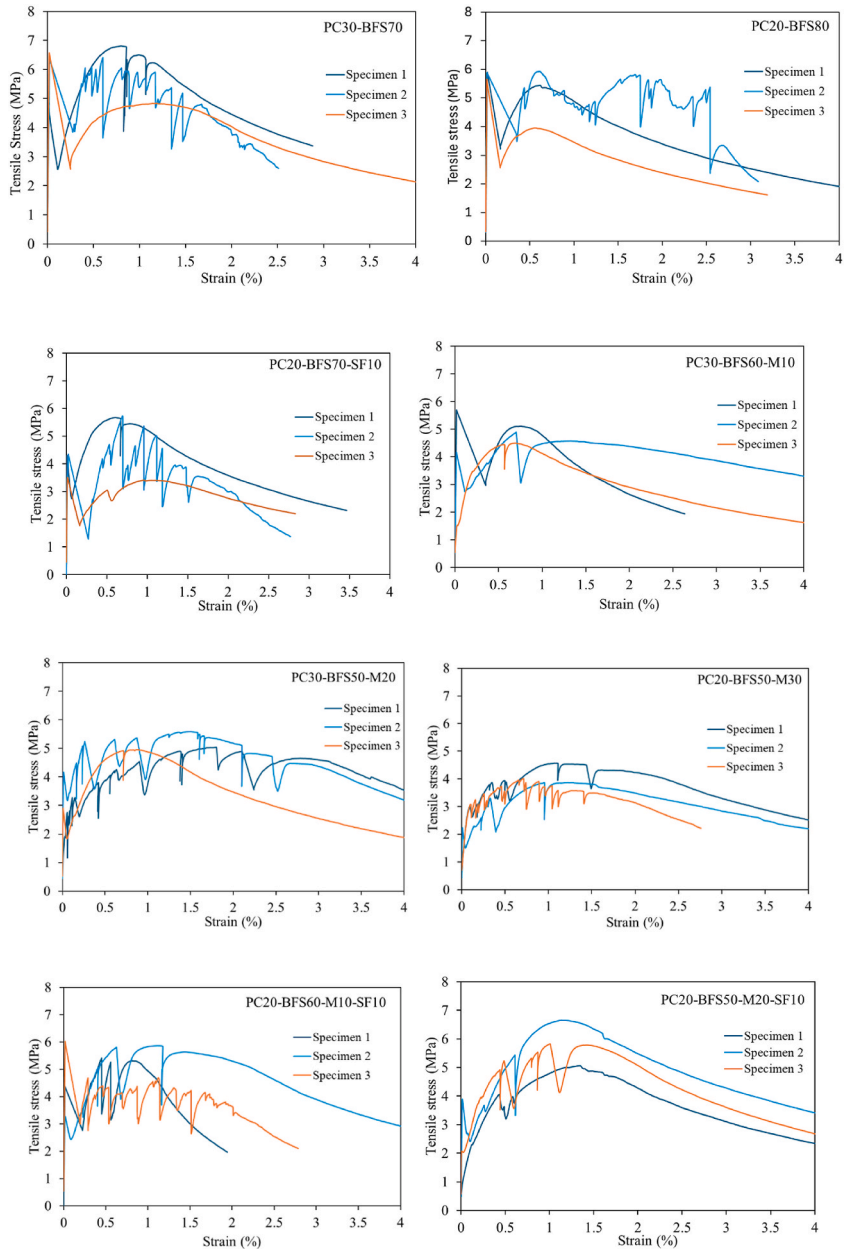


Fig. 3. Tensile stress-strain behaviour of the mixes considered in the study.

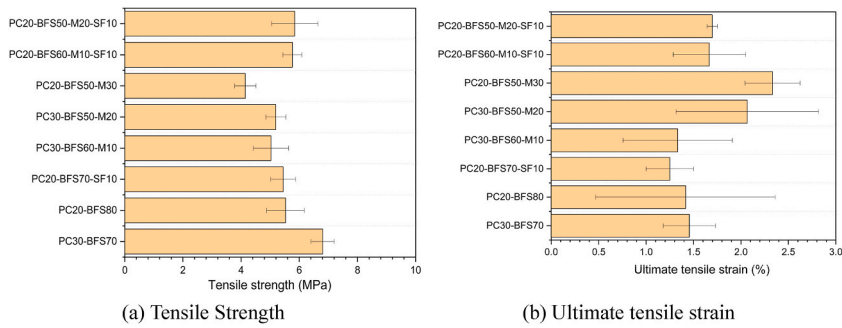


Fig. 4. Tensile strength and ultimate tensile strain of the considered mixes.

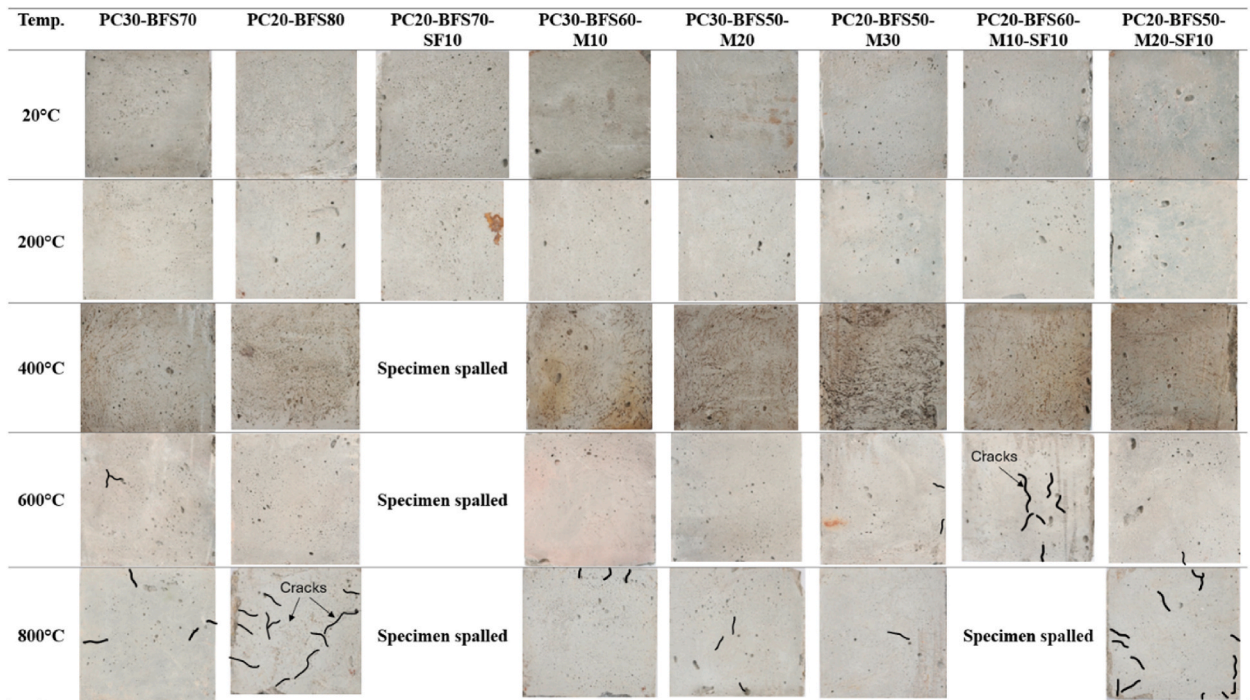


Fig. 5. Spalling and crack formation in different mixes at elevated temperatures.

which then peaked at 20 % MgO content. However, this effect was not significant when considering the standard deviation of the data. The effect becomes more pronounced with cement replacement. For instance, replacing an additional 10 % of cement with MgO (mix PC20-BFS50-M30) resulted in a 16.9 % reduction in compressive strength compared to mix PC30-BFS50-M20. This highlights the complex effects of GGBFS-MgO blends. Initially, replacing GGBFS with lower amounts of MgO (10–20 %) may have led to the formation of new hydration products, possibly brucite and M-S-H, which positively impacted strength. However, as MgO replacement increased, particularly as a substitute for cement, the formation of primary hydration products like C-S-H decreased due to the lower cement content, and the excess MgO may not have fully hydrated, leading to a reduction in strength. Nevertheless, this decrease could be minimized if MgO content was replaced with silica fume. Fig. 2(b) further illustrates the effect of adding MgO by comparing mixes with quaternary blends. Contrary to previous reports on the effect of MgO, it is observed that adding MgO may slightly increase compressive strength. The compressive strength of mix PC20-BFS60-M10-SF10 increased by 5 % when 10 % GGBFS was substituted with MgO. This indicates that MgO plays a positive role in enhancing strength, provided that a pozzolanic medium is still present. In this particular instance, silica fume proved beneficial as it potentially engaged in secondary pozzolanic reactions with GGBFS and MgO, while MgO might have also contributed to the densification of the matrix by filling some of the remaining pores in system. A more detailed explanation of the mechanism is provided in Section 5.

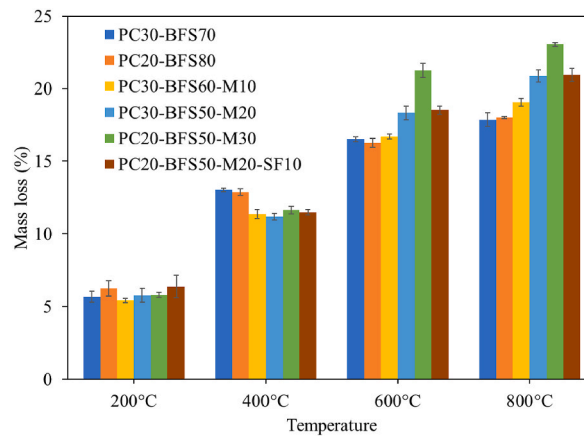


Fig. 6. Mass loss at elevated temperatures.

3.2. Tensile stress-strain behaviour

Fig. 3 shows the tensile stress-strain behaviour of the considered mixes. The strain hardening behaviour could be clearly observed with each curve demonstrating a steep rise at a very minimal strain, followed by consistent strain hardening. After reaching the peak tensile stress, the curves exhibited strain softening behaviour. This pattern was consistent across all mixes, regardless of the type or proportion of binder material.

Fig. 4 further shows the tensile strength and ultimate tensile strain of the developed composite. It can be observed from Fig. 4(a) that the tensile strength (peak tensile stress) followed the same trend as compressive strength. Replacing MgO with GGBFS resulted in a slight decrease in tensile strength, with the maximum tensile strength observed at 20 % MgO for the mix PC30-BFS50-M20. The tensile strength of this mix was approximately 23 % lower than that of mix PC30-BFS70, which did not contain any MgO. This indicates that MgO does not significantly enhance strength due to its lower pozzolanic activity. A further comparison can be drawn between mixes PC30-BFS50-M20 and PC20-BFS50-M20-SF10 which mainly differ in silica fume content. The corresponding strength confirms that the addition of silica fume (10 % replacement of cement) in the latter mix led to slight improvement in the tensile strength.

All the mixes also showed ultimate tensile strain higher than 1 % as shown in Fig. 4(b). The trend was somewhat inverse to that of tensile strength and the mixes with a higher replacement ratio or lower tensile strength demonstrated greater strain capacity. Mix PC20-BFS50-M30, which contained 30 % MgO, had the highest ultimate tensile strain at 2.3 %, while mix PC30-BFS70 had the lowest at 1.45 %. This may be attributed to the lower hydration degree of the corresponding mixes, as reflected in their compressive and tensile strengths. The chemical bond between PE fibre and matrix is believed to be influenced by the formation of a hydroxide layer in the ITZ [38]. Due to the low pozzolanic reaction, a strong bond was not possible, which might have enhanced the ultimate tensile strain without causing fibre rupture.

4. Mechanical performance at elevated temperatures

4.1. Spalling and crack propagation

Fig. 5 depicts the surface features of cubic samples exposed to different temperature ranges. Initially, at room temperature, the specimens appeared light grey, likely due to the presence of white GGBFS, MgO, and silica fume. As the temperature increased to 200 °C, all specimens became brighter in colour without any visible micro or major cracks. At 400 °C, the specimens exhibited a darker colour, possibly attributed to the polyethylene fibres, which tend to darken before vaporization [39]. Notably, when 10 % of cement was replaced by silica fume in the PC20-BFS70-SF10 mix, spalling occurred at 400 °C and higher temperatures. Moreover, with increasing temperature, micro-cracks also appeared in specimens containing silica fume. At 800 °C, severe spalling was observed in specimens with PC20-BFS70-SF10 and PC20-BFS60-M10-SF10 mixes, while major cracks were evident in specimens from the PC20-BFS50-M20-SF10 mix. Conversely, specimens without silica fume did not experience major cracking or spalling and only minor cracks were detected. This observation highlights that silica fume may not be suitable for high-temperature applications due to higher risk of spalling [25]. Unlike mixes with coarser SCMs, cementitious matrix containing silica fume lack a network of interconnected pores due to reduced permeability. This limits pathways for vapor release, intensifying the internal pressure and increasing the likelihood of spalling.

4.2. Mass loss

Fig. 6 shows the variation in mass loss of the considered mixes at temperature ranging from 200 to 800 °C. Mass loss data for specimens PC20-BFS70-SF10 and PC20-BFS60-M10-SF10 is not presented due to the spalling of the specimens. The results indicate an

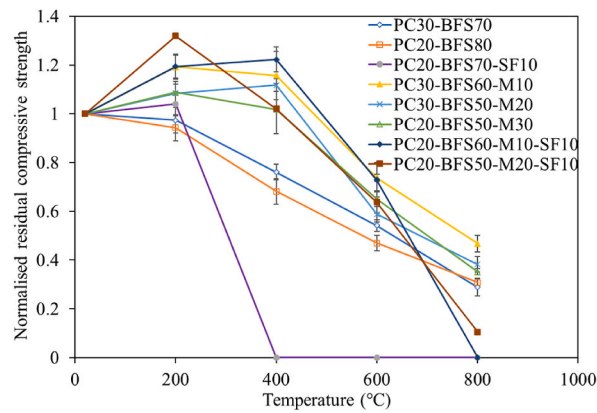


Fig. 7. Normalised residual compressive strength of the considered ECC mixes.

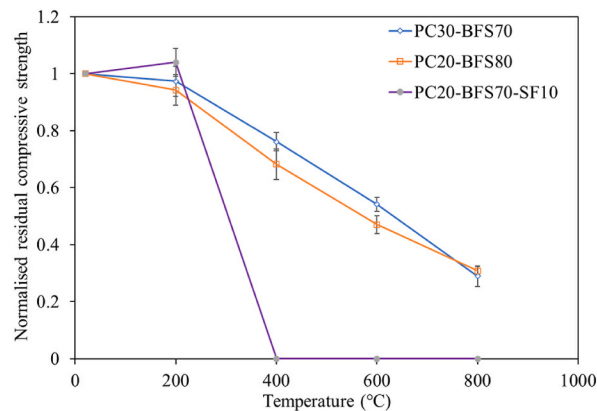


Fig. 8. Effect of GGBFS and SF on the residual compressive strength.

increase in mass loss with rising temperature, with similar trends observed across different mixes. At 200 °C, mass loss ranged from 5.4 % to 6.3 %, primarily due to specimen dehydration from the release of free and chemically bound water. On further increase in temperature to 400 °C, mass loss increased by 6 % with total mass loss ranging from 11.1 to 13 %. This trend continued up to 600 °C, with a further 5–6% increase, resulting in a mass loss range of 16.2%–21.3 %. From 600 to 800 °C, the mass loss increased slightly by 2 %, reaching a total of 17–23 %. Mass loss remained consistent across the mixes, though those with higher MgO content showed increased loss after 400 °C, likely due to the decomposition of brucite and other hydration phases. This may explain the notably higher mass loss in PC20-BF50-M30, containing 30 % MgO. Overall, the mass loss variation was similar to that observed in common types of ECC, indicating minimal impact from the inclusion of higher amounts of GGBFS and MgO in terms of damage associated with increased mass loss.

4.3. Residual compressive strength

Fig. 7 shows the normalised residual compressive strength of all mixes after exposure to temperature ranging from 200 °C to 800 °C. Irrespective of the binder type or dosage, it is evident that compressive strength decreases as temperature increases, with a significant drop at 800 °C. This aligns with findings from other studies, indicating that such high temperatures severely damage the microstructure of cementitious composites [25]. At this temperature, the decomposition of hydration products is nearly complete, making it difficult to retain strength and resulting in lower percentage retention. However, the extent of decomposition varies with the type of matrix, suggesting that choosing an appropriate binder can lead to higher strength retention. For instance, at 800 °C, the mix PC30-BFS60-M10, containing 60 % GGBFS and 10 % MgO, retained about 47 % of its strength, while the mix with silica fume experienced a significant strength reduction and even spalling in some cases. The effect of each SCM is further discussed below.

4.3.1. Effect of GGBFS

Comparison of the residual compressive strength of mixes with GGBFS and silica fume is demonstrated through Fig. 8. It can be observed that mix with 70 % and 80 % GGBFS contents suffered continual decrease in residual compressive strength with increase in temperature. However, on replacing GGBFS with 10 % silica fume in mix PC20-BFS70-SF10, there was slight increase in strength at

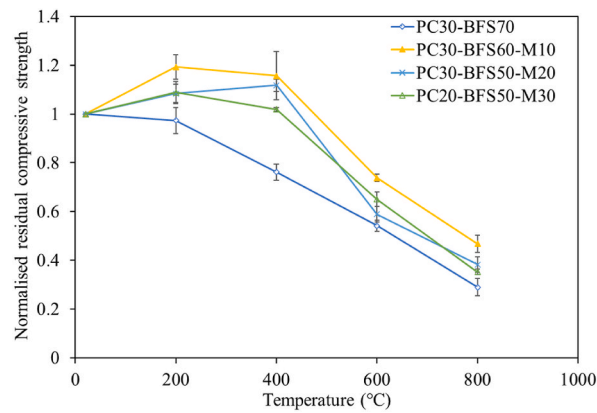


Fig. 9. Effect of MgO content on the residual compressive strength.

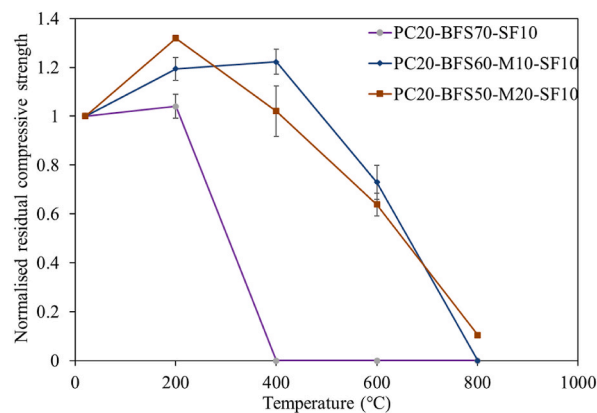


Fig. 10. Residual compressive strength of quaternary blended ECC mixes.

200 °C. This increase could be due to the accelerated pozzolanic reaction between silica fume and cement or GGBFS, where water vapor moving inward within the cube reacts with cementitious materials to enhance hydration [40,41]. It should be noted that the silica fume mix did not perform well beyond 200 °C, with all specimens spalling as described earlier. For mixes containing only GGBFS, an increase in GGBFS content led to a decrease in strength retention capacity. The mix with 70 % GGBFS (PC30-BFS70) retained approximately 76 % and 54 % of its strength at 400 °C and 600 °C, respectively, while the mix with 80 % GGBFS (PC20-BFS80) retained 68 % and 47 %. At 800 °C, both mixes showed similar strength. The initial difference in strength retention may be due to the higher amount of hydration products (C-S-H) in the mix with more cement, which helped it retain strength better, as the decomposition of C-S-H is only complete after 600 °C. In mixes with higher GGBFS content, C-S-H formation may have been slower, as indicated by their room temperature strength, leading to lower strength retention.

4.3.2. Effect of MgO

The effect of addition of MgO can be further understood from Fig. 9. It can be observed that MgO is positive for achieving higher strength retention at elevated temperatures. All the mixes containing MgO outperformed the PC30-BFS70 mix, irrespective of the MgO amount. Notably, mixes with MgO also exhibited an initial increase in strength at 200 °C. Compressive strength of the mix PC30-BFS60-M10, PC30-BFS50-M20 and PC20-BFS50-M30 was 19.3 %, 8.4 % and 8.8 % higher respectively at 200 °C than the room temperature strength. Although there was a slight decrease in strength after 200 °C, the residual compressive strength still remained higher than that at the room temperature. This may have been due to accelerated hydration and internal autoclaving, leading to more hydration products, including brucite. After 400 °C, the mixes with MgO experienced a significant strength decrease, possibly due to brucite decomposition; however, their strength was still higher than the PC30-BFS70 mix without MgO. Mix PC30-BFS60-M10 was found to retain around 46.7 % strength at 800 °C which was the highest among all the considered mixes, whereas the strength retention of mix PC30-BFS70 without MgO was just 28.9 %.

4.3.3. Effect of silica fume and MgO blends

Further analysis of the mixes containing blends of MgO, and silica fume is illustrated using Fig. 10. It is evident from the previous section that the mix containing 10 % silica fume (added as a replacement of GGBFS) suffered spalling at 400 °C and above. However,

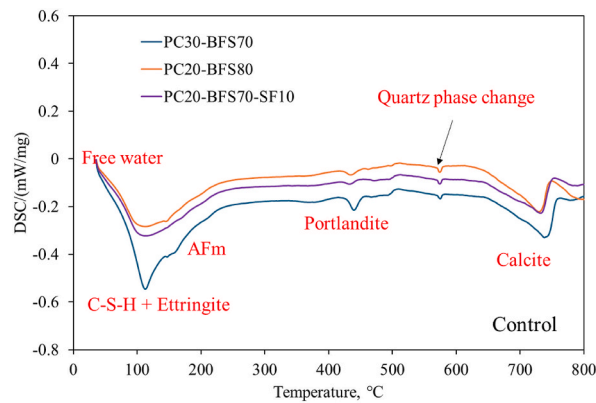


Fig. 11. Effect of GGBFS and SF at room temperature using DSC analysis (with upward peaks denoting exothermic reaction).

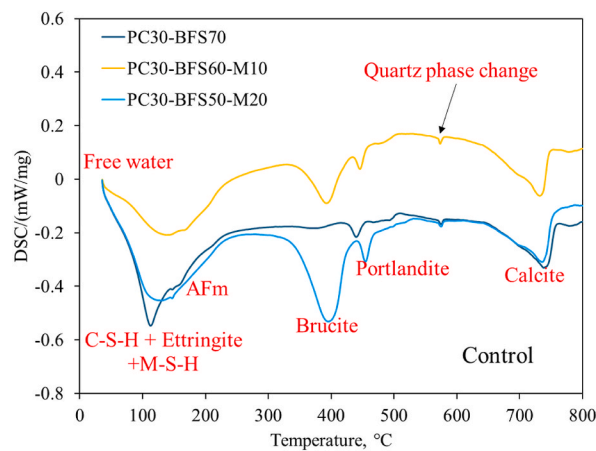


Fig. 12. Effect of MgO dosage at room temperature using DSC analysis (with upward peaks denoting exothermic reaction).

this performance could be significantly enhanced by incorporating MgO as a replacement for GGBFS. In the case of 10 % replacement (mix PC20-BFS60-M10-SF10), not only did spalling resistance improve considerably, but strength retention was also higher across all temperatures. At 200 °C, mix PC20-BFS60-M10-SF10 demonstrated approximately 19 % increase in strength, compared to just 4 % increase in mix PC20-BFS70-SF10 which did not contain MgO. This increase further improved on increasing the dosage of MgO. For mix PC20-BFS50-M20-SF10, strength increase was around 31 % which was highest among all the mixes considered in the study. This indicates that accelerated hydration depends on the individual composition of all SCMs, and the right selection of binder material can enhance performance. Both PC20-BFS60-M10-SF10 and PC20-BFS50-M20-SF10 with MgO demonstrated improved performance up to 400 °C, but performance significantly deteriorated beyond that. At 800 °C, mix with just 10 % MgO suffered spalling, whereas the mix with 20 % MgO showed just 10 % strength retention which was much lower than the mixes without silica fume. These findings again validates that the presence of silica fume is not beneficial for elevated temperature applications.

5. Effect of SCM addition through microstructure evolution

5.1. Room temperature

The effect of each constituent can be further understood from the detailed microstructural analysis as described hereafter. In particular, DSC curves reveal three notable endothermic heat flow peaks. The first peak in the temperature interval from 50 °C to 250 °C corresponds to the release of free water, physically bound water from pores, together with the dehydration reactions due to the loss of water from C-S-H, M-S-H, ettringite and AFm phase. The second peak, between 420 °C and 520 °C, represents the decomposition of portlandite, while the third peak, from 650 °C to 800 °C, corresponds to the decomposition of calcite. It can be clearly observed from Fig. 11 that as the slag replacement ratio increased from 70 % (in mix PC30-BFS70) to 80 % (in mix PC20-BFS80), the energy released during the decomposition of the first peak compounds decreased, indicating incomplete hydration. This suggests that higher slag ratios hinder the complete formation of hydration products, resulting in lower observed strength. The addition of silica fume slightly improved the decomposition observed in the first peak, suggesting that silica fume might react with the portlandite

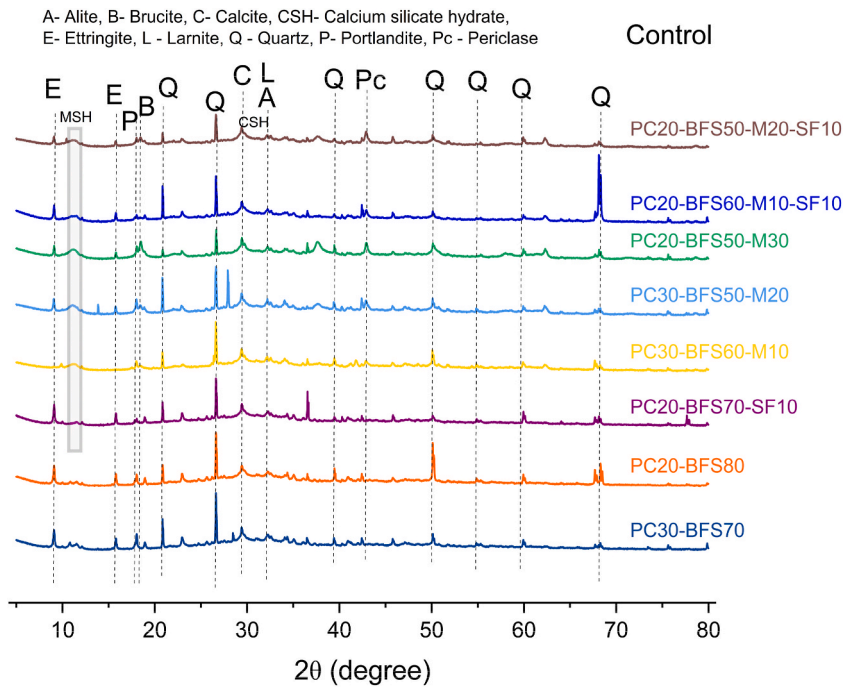


Fig. 13. X-ray diffractograms of different ECC mixes at room temperature.

present in the system to generate additional hydration compounds. Consequently, the strength was slightly higher with the addition of silica fume.

The effect of MgO at room temperature can be better understood from Fig. 12. In addition to all the aforementioned peaks, the mixes containing MgO also showed a peak from around 350–400 °C due to the presence of brucite and the intensity and width of this peak increased with increase in the MgO percentage. This may have been the reason of a broad peak of brucite in mix PC20-BFS50-M20. The trend of strength was PC30-BFS70 > PC30-BFS60-M20 > PC30-BFS60-M10 could also be related to the area of first decomposition peak. This decomposition area followed the same order, indicating the presence of hydration compounds in mix PC30-BFS50-M20 with 20 % MgO compared to mix PC30-BFS60-M10 which could be possibly due to more M-S-H. Moreover, the presence of different sized SCMs, along with the formation of brucite leading to better particle packing may have collectively contributed to the increased strength due to the presence of MgO.

XRD analysis was performed to further understand the variation pattern. As observed from DSC analysis, several key hydration phases are present, and their corresponding XRD peaks can provide additional insight into the microstructural evolution. The main peaks are shown in Fig. 13. In general, calcite displays strong diffraction peaks around $2\theta \sim 29.4^\circ$, while C-S-H may exhibit a broad diffraction peak around 29° due to its disordered nature, resulting in an overlap resembling a hump, as illustrated in Fig. 13. Additionally, ettringite shows an intense peak around 9.1° , and portlandite around 18.4° , with the brucite peak closely resembling that of portlandite. The broad peak between 10 and 13° may be assigned to M-S-H [42]. All these compounds contribute to strength either by participating in primary or secondary hydration reactions or by contributing to better particle packing. Comparing mixes with a high volume of GGBFS (PC30-BFS70 and PC20-BFS80), the portlandite peak and C-S-H hump appear slightly more intense in PC30-BFS70, indicating their higher presence. This is consistent with the DSC results and might explain the superior compressive strength of the PC30-BFS70 mix compared to PC20-BFS80, which showed a reduced hydration at the first decomposition peak. The intensity of C-S-H somewhat improved with the addition of 10 % SF in the PC20-BFS70-SF10 mix, potentially contributing to its slightly higher strength. However, the portlandite intensity appears slightly lower in the mix with SF, suggesting that the mix with a higher volume of GGBFS (PC20-BFS80) may gain strength over the long term. Portlandite can act as a reservoir of water within the concrete matrix, aiding in internal curing and consequently, strength development. Similarly, for mixes containing MgO, the periclase peak is highest in the PC20-BFS50-M30 mix which is expectedly due to the presence of high amount of MgO. M-S-H peak is also visible for these mixes. Though both M-S-H and brucite was formed in this mix, a larger amount of MgO may still have been left unreacted. The periclase intensity decreased with decrease in the MgO content in the mix. However, the portlandite peak is most intense for the PC30-BFS50-M20 mix, and M-S-H is also prominently present, likely contributing to its higher strength as observed in compressive strength tests.

5.2. Changes between 200 and 400 °C

Fig. 14 shows the X-ray diffraction pattern of specimens after 200 °C. It can be seen that the ettringite peaks have disappeared in all

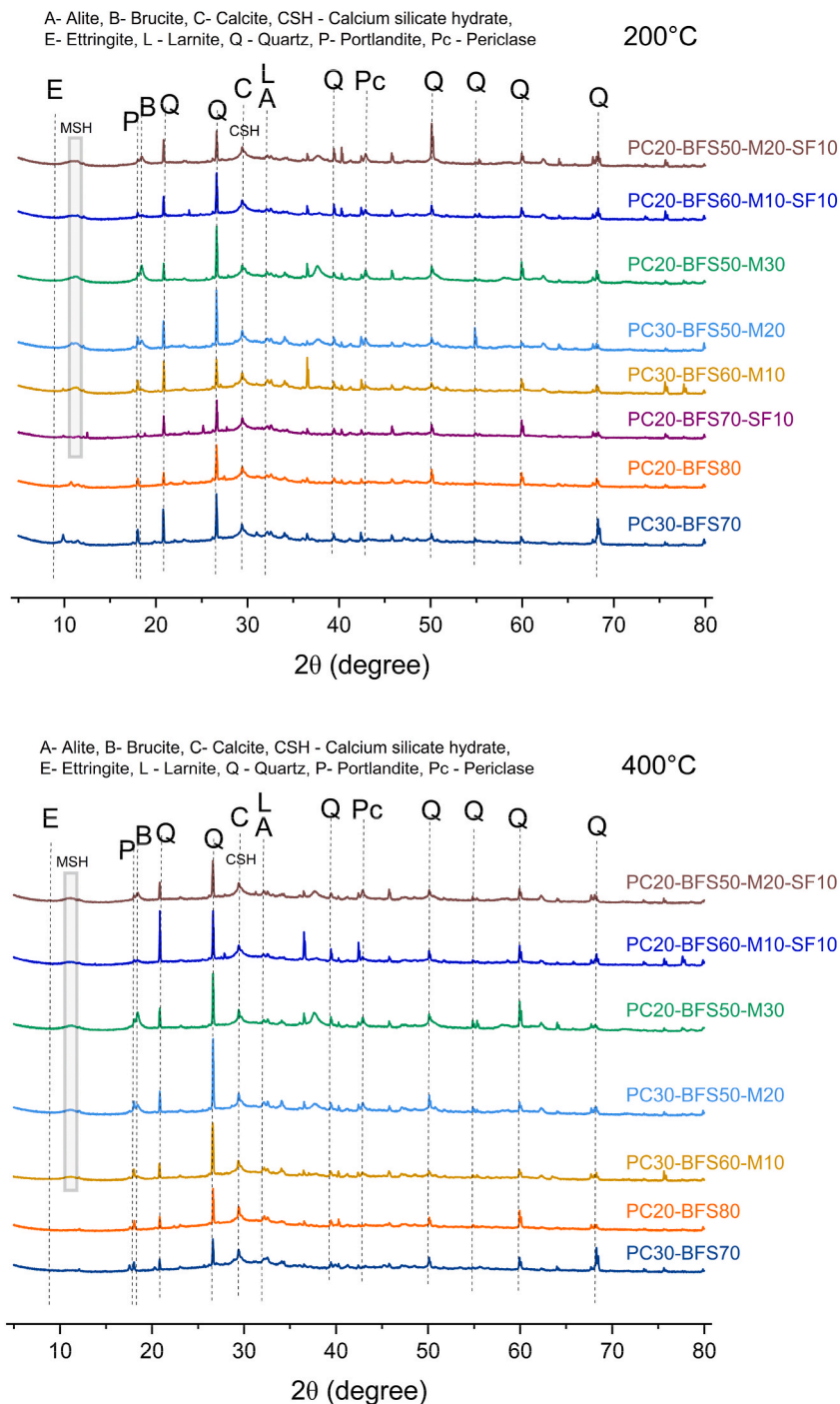


Fig. 14. X-ray diffractograms of different ECC mixes at 200 °C and 400 °C.

the specimens indicating possible decomposition. However, the portlandite peaks are still visible with varying intensity and the broad diffraction peak of C-S-H and M-S-H could still be seen. The intensity of portlandite and MgO peak varied and were lesser than that observed at room temperature, possibly indicating their partial involvement in secondary hydration. If compared among the mixes, it is observed that the mixes with only cement and GGBFS did not undergo any initial gain in strength even though the portlandite has been seen to be consumed. The initial strength is maximum in mixes with SF and MgO blends which shows that the effect of binary and ternary blend is more effective due to enhanced hydration and compactness it may lead during the initial increase in temperature. This may also be due to the retarding effect of MgO allowing for better formation and growth of new hydration products at later stage even

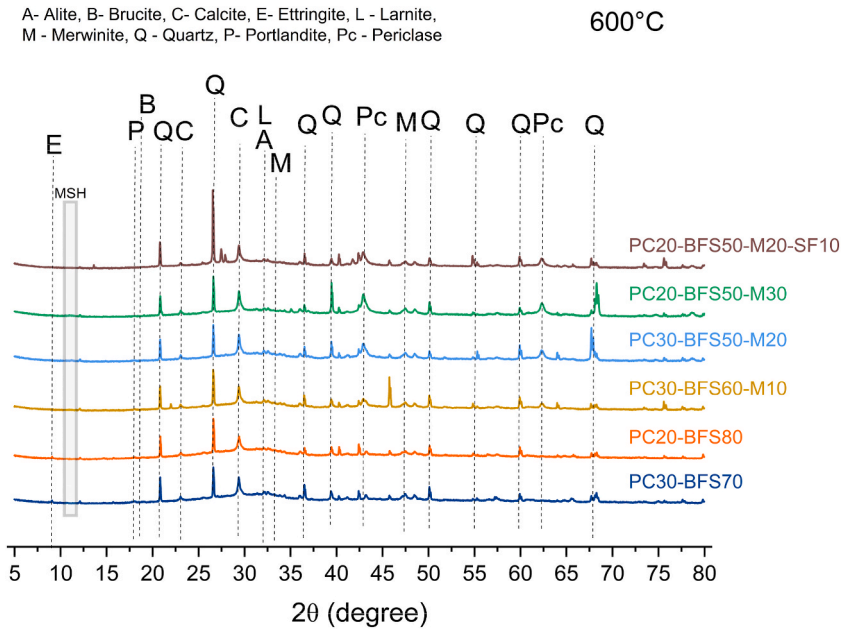


Fig. 15. X-ray diffractograms of different ECC mixes at 600 °C.

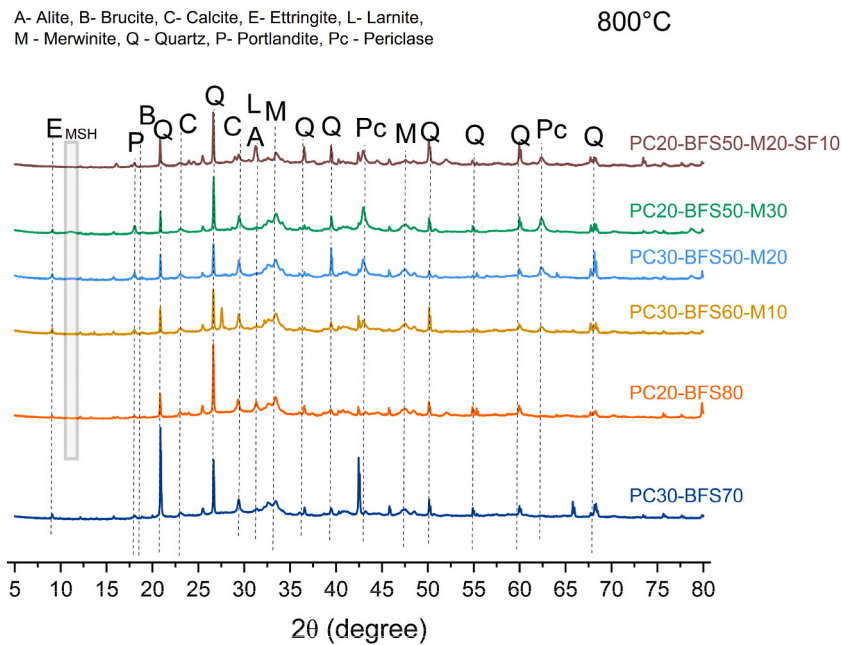


Fig. 16. X-ray diffractograms of different ECC mixes at 800 °C.

when after the decomposition of exiting products partially started. This effect likely contributed to the highest strength gain in mix PC20-BFS50-M20-SF10 showing around 31 % strength increase at 200 °C. A similar effect was observed with further increase in temperature to 400 °C.

5.3. Effect at 600–800 °C

On further increase in temperature to 600 °C, both portlandite and brucite disappears as seen from Fig. 15. However, it should be noted that C-S-H broad diffraction peak is still visible potentially suggesting the higher strength shown by mixes till this temperature. Mixes with higher amount of MgO showed distinct periclase peak which might have been due to the decomposition of brucite to MgO.

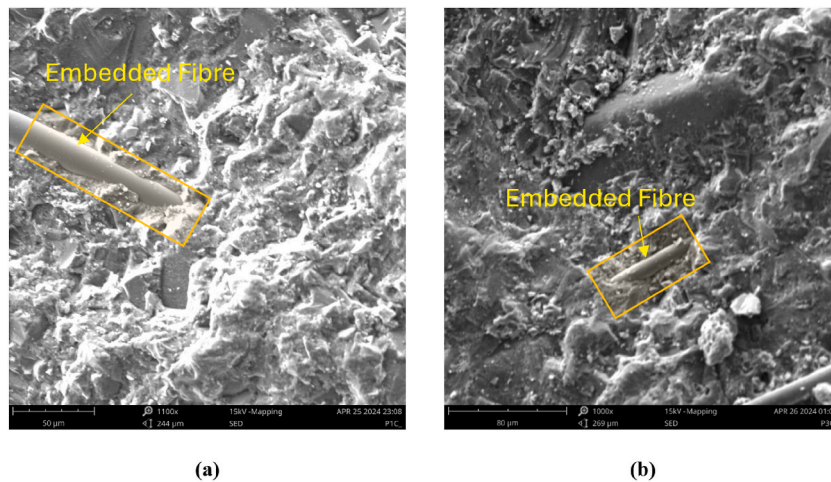


Fig. 17. Fibre-matrix interface in mix (a) PC30-BFS70 and (b) PC30-BFS50-M20 at room temperature.

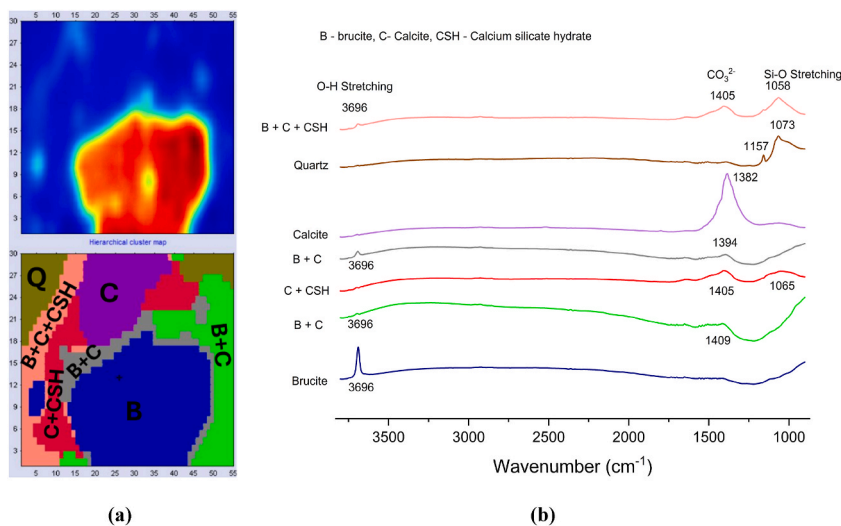


Fig. 18. Synchrotron ATR-FTIR analysis of ITZ between MgO and PC30-BFS50-M20 matrix: (a) synchrotron ATR-FTIR chemical image of brucite peak at 3696 cm^{-1} (top) and its corresponding HCA map with 7 clusters revealing the ITZ features (bottom); (b) representative average ATR-FTIR spectra extracted from each HCA cluster and presented in their corresponding colours.

The peaks of alite and larnite remains similar to the control specimens indicating that the decomposition of Ca-phases has not yet fully started.

Fig. 16 shows the X-ray diffractograms of the considered mixes at $800\text{ }^{\circ}\text{C}$. It can be seen that C-S-H hump is not visible anymore indicating its complete decomposition and thereby the possible drastic strength decrease. However, portlandite and ettringite peaks reappears again but at very lower intensity. These compounds may have formed due to rehydration during the cooling process after exposure to high temperatures. At higher temperature, there is a high likelihood of hydration phase decomposition into CaO which may lead to further rehydration and subsequently the formation of ettringite and portlandite due to its strong affinity with water. This also shows the potential of rehydration in high volume GGBFS specimens. In regard to the effect of MgO, it can be seen that sharp peaks of periclase are visible with intensity increasing with increase in the content of MgO in the original mix. Moreover, presence of Alite is also lower. However, no peaks of brucite are detected in mixes containing MgO, likely due to the slower reaction rate of MgO with water. Interestingly, the X-ray diffractograms of all the mixes showed merwinite as one of the phases which is typically associated with slag melting and quenching. In the present case, this phase may have been the result of the heat exposure. The highest intensity of Alite-belite phases is seen in PC20-BFS50-M20-SF10 followed by PC20-BFS80 indicating a significant amount of decomposition and hence, the observed lower strength.

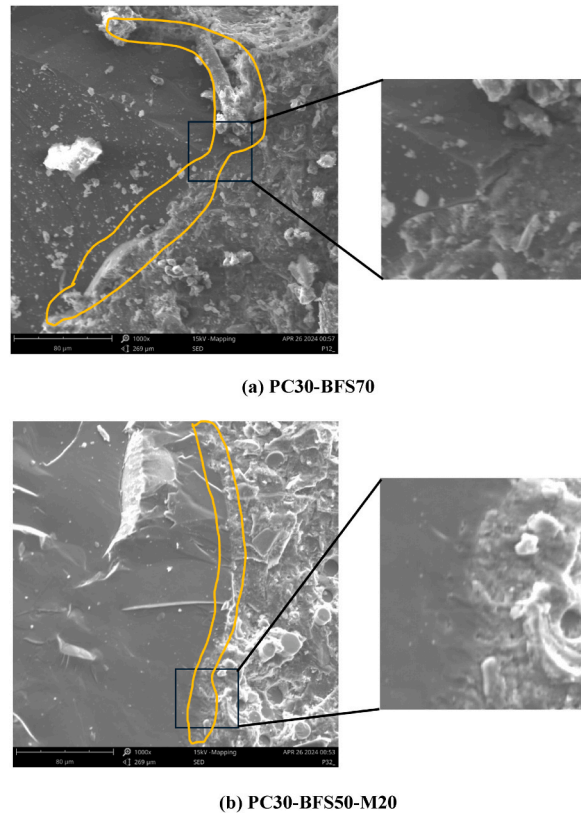


Fig. 19. ITZ at 200 °C in mix (a) PC30-BFS70 and (b) PC30-BFS50-M20.

6. ITZ and crack formation at different temperature ranges

6.1. Room temperature

In terms of the interface, high volume GGBFS blended matrix with and without MgO showed strong interface between aggregate and matrix as well as between the fibre and matrix, indicating that the ITZ is not significantly affected due to the presence of GGBFS or MgO. This observation is supported by SEM micrographs of PC30-BFS70 and PC30-BFS50-M20 at room temperature (Fig. 17), which reveal that the ITZ around the matrix and the fibre remained dense and compact.

The role of MgO and its surrounding surface was further analysed using synchrotron ATR-FTIR microspectroscopy to provide chemical distribution at interfaces of the mix PC30-BFS50-M20. A high-resolution HCA image was generated based on the synchrotron ATR-FTIR map using 7 clusters, showing chemical information of interfaces surrounding the brucite crystal (Fig. 18) with representative average ATR-FTIR spectra extracted from each cluster and presented in their corresponding colours for chemical identification and comparison purposes. According to the HCA image, the region adjacent to the brucite contained both brucite and calcite. In particular, the chemical fingerprints characteristic to C-S-H were evident in the ATR-FTIR spectra, suggesting its bonding and co-existence with brucite and calcite components as interfaces between quartz, calcite and brucite as seen in pink and red clusters. The C-S-H bonding at interfaces could therefore play a key role in providing strong interfacial interactions between the brucite, calcite, and quartz crystals with no voids. This clearly demonstrate that the hydrated MgO can remain densely packed within the blended matrix and likely contributes to the high strength as observed through compressive performance analysis.

6.2. Elevated temperatures

Analysing variations in the ITZ and crack development in matrix at elevated temperatures is crucial as it significantly influences the resulting strength. The compressive strength saw a slight increase in mixes containing MgO at 200 °C. During this initial temperature rise, the evaporation of interlayer water within the C-S-H structure may lead to a decrease in the surface area of C-S-H, contributing to densification and subsequently increased strength. The degree of densification may vary depending on the type of matrix, with MgO-doped matrices exhibiting better interfaces. This can be further shown from the ITZ analysis of the PC30-BFS70 and PC30-BFS50-M20 with only difference in MgO content using Fig. 19. It can be observed that a strong interface still exists in MgO based mixes unlike the mixes without MgO. A higher amount of MgO may have lowered the degree of hydration at initial stage, which was later accelerated at

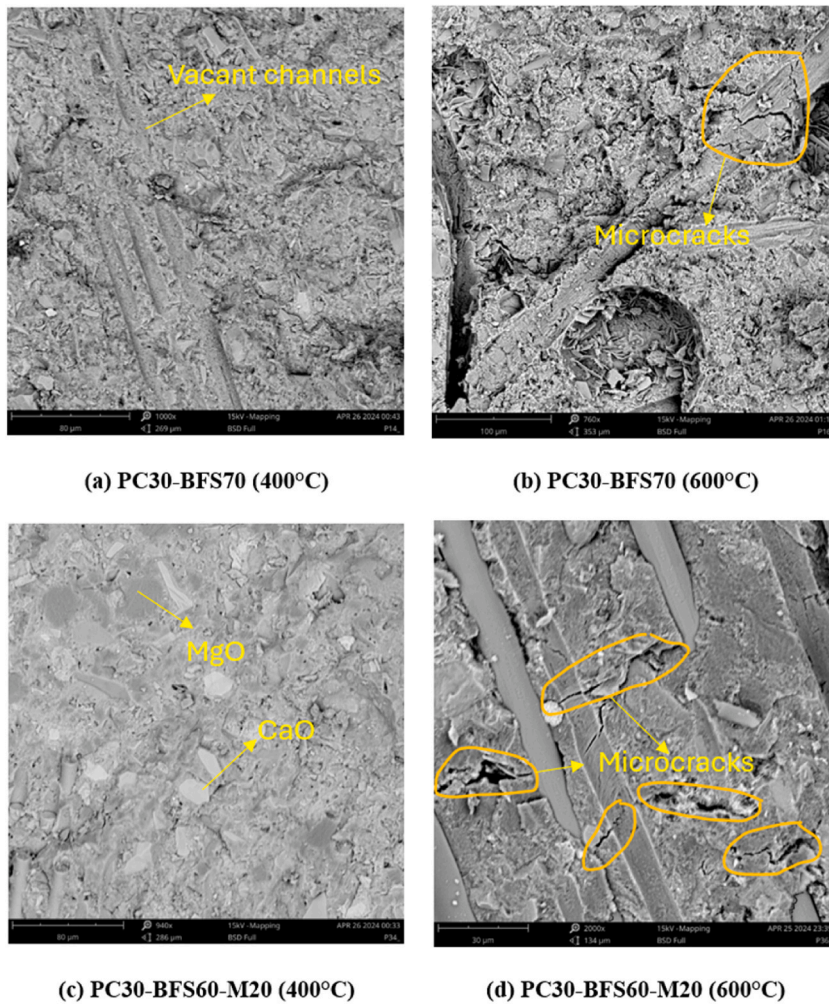


Fig. 20. Variation in mix (a/b) PC30-BFS70 and (c/d) PC30-BFS50-M20 at 400 °C and 600 °C.

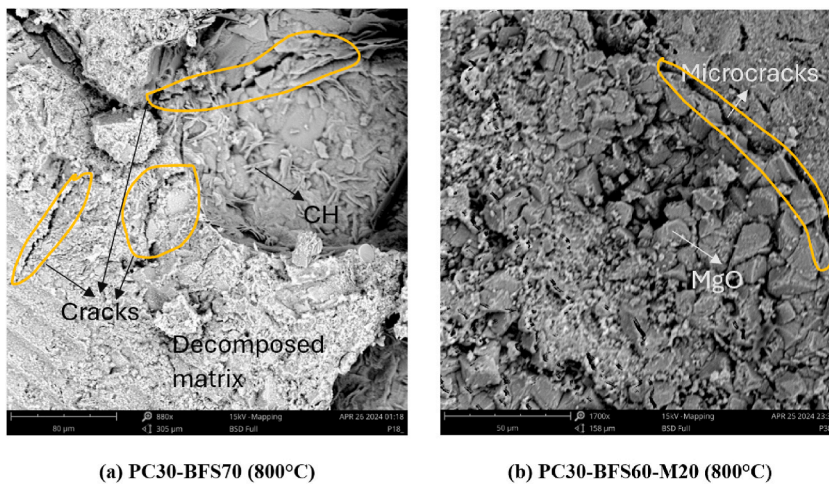


Fig. 21. Variation in mix (a) PC30-BFS70 and (b) PC30-BFS50-M20 at 800 °C.

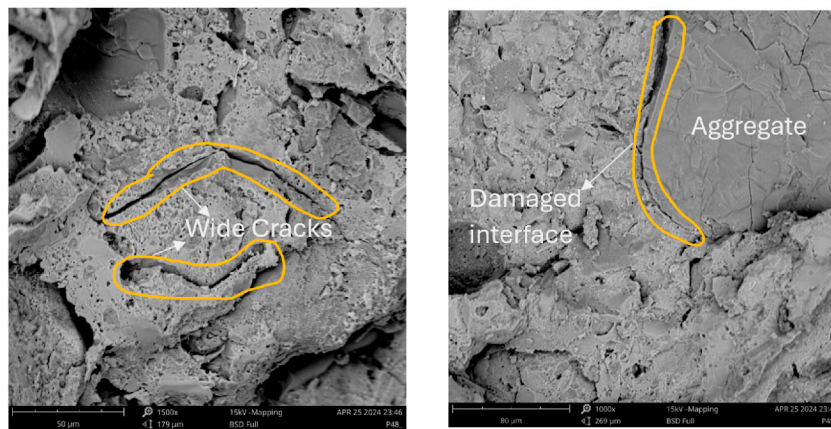


Fig. 22. Mix PC20-BFS60-M10-SF10 at 800 °C.

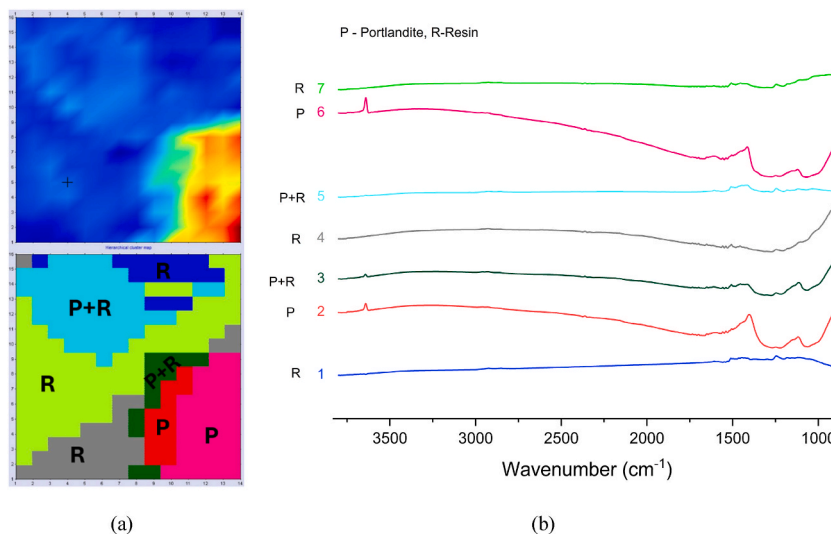


Fig. 23. Synchrotron ATR-FTIR analysis of ITZ in PC30-BFS50-M20 matrix at 800 °C: (a) synchrotron ATR-FTIR chemical image of portlandite peak at $\sim 1400\text{ cm}^{-1}$ (top) and its corresponding HCA map with 7 clusters revealing the ITZ features (bottom); (b) representative average ATR-FTIR spectra extracted from each HCA cluster and presented in their corresponding colours.

this temperature and hence, a compact matrix was seen. This was also confirmed through XRD and DSC analyses as explained in the previous section.

As the temperature increased within the range of 400–600 °C, the dehydroxylation process of C-S-H took place, leading to an increase in porosity and the potential formation of microcracks. Consequently, there was a significant decline in strength observed across all mixes. The extent of this decrease depended on the porous structure and the extent of microcracks. Vacant channels or decomposed MgO and CaO particles are seen within the matrix at 400 °C, however there is no clear evidence of cracks (Fig. 20 a/c). On the other hand, at 600 °C, cracks were clearly observed near vacant channels, contributing more significantly to the observed drop in strength, as clearly indicated in Fig. 20(b/d). This phenomenon was observed consistently across all mixes irrespective of the composition.

On further increase in temperature to 800 °C, the C-S-H tends towards complete decomposition to $\beta\text{-C}_3\text{S}$ and $\beta\text{-C}_2\text{S}$. These phases exhibit less hydration and greater crystallinity compared to C-S-H, resulting in specimens with an extensively porous profile. The strength decrease was higher possibly due to the porous nature of the decomposed matrix and the relative variation may have been dependent on the microcracks. It can be seen from Fig. 21 that microcracks are clearly visible in the matrix. CH can also be found in the matrix as also observed through XRD which may have been due to rehydration. Further comparison with mixes containing silica fume (PC20-BFS60-M10-SF10) in Fig. 22 supports the presence of wide cracks and damaged interfaces between aggregate and matrix, likely resulting from the explosive spalling behaviour.

High-resolution synchrotron ATR-FTIR measurement was again performed on the PC30-BFS50-M20 specimens after being treated at 800 °C, to gain further insights into the observed poor strength. Fig. 23 presents the resultant HCA image containing 7 clusters

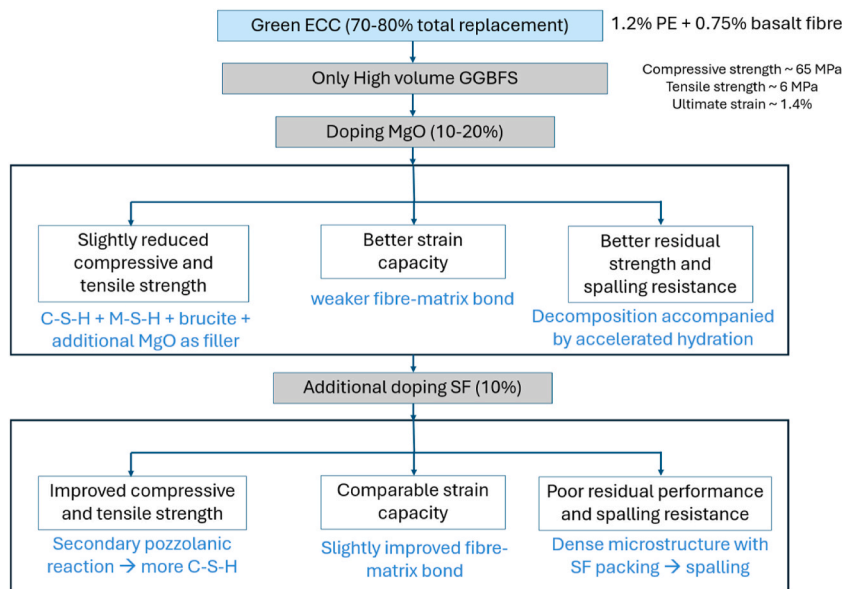


Fig. 24. Effect of MgO and SF doping in high volume GGBFS ECC matrix.

generated based on the synchrotron ATR-FTIR map of the PC30-BFS50-M20 specimen at 800 °C, which reveal chemical signatures of epoxy resin dominating a large area around the portlandite matrix (product of rehydration). Due to the strong presence of microcracks and pores observed in this specimen, it is likely that the epoxy resin (used as an embedding medium for cutting/polishing purposes) infiltrated into the main matrix of the specimen and filled up pores and gaps during the sample preparation process. While the specimen prepared at room temperature revealed no presence of epoxy resin and provided strong interface leading to a high strength, SEM analysis of the specimens subjected to 800 °C showed the visual damage of interfaces in forms of microcracks and pores, which is further confirmed by the presence of epoxy resin. This damage notably caused the poor strength across all the mixes.

Considering the positive impact of MgO on shrinkage reduction as evident from the existing studies [18,23] and the superior mechanical performance as obtained in the present study, it can be confirmed that MgO may be an effective doping material in high-volume SCM matrices. The overall mechanism and optimal dosage for enhancing the performance of high-volume GGBFS matrices doped with MgO and silica fume at room and elevated temperatures are summarized in Fig. 24.

7. Conclusions

This study investigated the role of MgO in high volume GGBFS matrix and its effect on the compressive and tensile stress-strain behaviour at room temperature and residual compressive strength at elevated temperatures. Detailed analysis on how the strength and microstructure evolves at elevated temperature in this unique matrix was also performed. It was observed that with 10–20% MgO doping in high volume GGBFS matrix, a superior performance at both room temperature and elevated temperatures could be obtained. Based on the findings, the following conclusions can be drawn:

- Mix with 70–80% GGBFS showed good performance with compressive strength >65 MPa, tensile strength >6 MPa and ultimate tensile strain >1.4%. Moreover, this use of high volume of GGBFS was also found effective at elevated temperature for high strength retention (~30% retention at 800 °C) without any observed spalling. Additionally, partial replacement of GGBFS with 10% SF though led to an improved performance at 200 °C, spalling was observed at later stages of temperature rise specifically after 400 °C.
- The addition of MgO enhanced tensile stress-strain behaviour, with distinct strain hardening and higher ultimate tensile strain observed in composites with higher MgO content. However, the compressive strength was slightly decreased.
- At elevated temperatures, the MgO-doped matrix showed better performance, with more than 40% strength retention at 800 °C. This improvement was attributed to the retarding effect of MgO, which may have accelerated hydration at later stages, resulting in significantly higher strength at 200 °C. MgO-based composites also exhibited better strength than their room temperature performance up to 400 °C.
- Microstructural analysis further revealed a strong interface between brucite (hydration product of MgO) and other hydration compounds, with clear presence of C-S-H which likely contributed to improved compressive performance. M-S-H was also identified in the MgO based matrix. Moreover, MgO was observed to undergo accelerated hydration at 200 °C, leading to higher strength. SF presence did not significantly influence M-S-H formation, but secondary pozzolanic reactions resulted in increased C-S-H content, potentially also contributing to higher strength at room temperature.

- Overall, 10–20 % MgO dosage with 70 % total replacement was found to be optimal for achieving very high compressive strength (63–66 MPa) and improved sustainability. Future research should focus on investigating the expansion characteristics of MgO, particularly in the presence of high amounts of SCM, to better understand its long-term effects on durability, cracking, and the confirmation of optimal dosage for specific applications.

CRedit authorship contribution statement

S. Rawat: Writing – original draft, Validation, Methodology, Investigation, Formal analysis, Data curation, Conceptualization. **Jitraporn Vongsivut:** Writing – review & editing, Resources, Methodology, Formal analysis. **Lihai Zhang:** Writing – review & editing, Supervision, Methodology, Funding acquisition. **Y.X. Zhang:** Writing – review & editing, Supervision, Resources, Project administration, Methodology, Funding acquisition, Conceptualization.

Declaration of competing interest

The authors declare that they have no known competing financial interests or personal relationships that could have appeared to influence the work reported in this paper.

Acknowledgement

This research was funded by the Australian Government through Australian Research Council Discovery Project (DP220103043). The support of the IRM beamline at the Australian Synchrotron, part of ANSTO, Australia through Grant no AS241/IRM/21168 is also acknowledged. The authors would also like to acknowledge the Advanced Materials Characterization Facility (AMCF) of Western Sydney University for access to its instrumentation and staff.

Data availability

Data will be made available on request.

References

- [1] V.C. Li, On engineered cementitious composites (ECC) a review of the material and its applications, *J. Adv. Concr. Technol.* 1 (3) (2003) 215–230.
- [2] M. Singh, B. Saini, H.D. Chalak, Performance and composition analysis of engineered cementitious composite (ECC)–A review, *J. Build. Eng.* 26 (2019) 100851.
- [3] M. Şahmaran, V.C. Li, De-icing salt scaling resistance of mechanically loaded engineered cementitious composites, *Cement Concr. Res.* 37 (7) (2007) 1035–1046.
- [4] M. Şahmaran, V.C. Li, Durability of mechanically loaded engineered cementitious composites under highly alkaline environments, *Cement Concr. Compos.* 30 (2) (2008) 72–81.
- [5] H. Liu, Q. Zhang, V. Li, H. Su, C. Gu, Durability study on engineered cementitious composites (ECC) under sulfate and chloride environment, *Construct. Build. Mater.* 133 (2017) 171–181.
- [6] Y. Zhu, Y. Yang, Y. Yao, Use of slag to improve mechanical properties of engineered cementitious composites (ECCs) with high volumes of fly ash, *Construct. Build. Mater.* 36 (2012) 1076–1081.
- [7] C. Liang, X. Liu, Y. Zhang, Z. Zhang, Z. Ma, Development of eco-friendly engineered cementitious composites (ECC) with both waste glass powder and aggregate: a comprehensive investigation, *J. Build. Eng.* 95 (2024) 110339.
- [8] K.T. Yan, L.Z. Li, J.H. Ye, D. Bazarov, B.Y. Deng, K.Q. Yu, Anisotropic size effect of 3D printed LC3-based engineered cementitious composites (LC3-ECC), *J. Build. Eng.* 92 (2024) 109668.
- [9] J. Yu, C. Lu, C.K. Leung, G. Li, Mechanical properties of green structural concrete with ultrahigh-volume fly ash, *Construct. Build. Mater.* 147 (2017) 510–518.
- [10] A. Al-Fakih, M.A. Al-Shugaa, M.A. Al-Osta, B.S. Thomas, Mechanical, environmental, and economic performance of engineered cementitious composite incorporated limestone calcined clay cement: a review, *J. Build. Eng.* (2023) 107901.
- [11] A. Saljoughian, H. Bahmani, Z. Ansari, N. Jafari, D. Mostofinejad, An eco-friendly ECC with high slag and polypropylene fiber content for high-tensile strain applications, *J. Build. Eng.* 91 (2024) 109726.
- [12] S. Rawat, Y.X. Zhang, C.K. Lee, Multi-response optimization of hybrid fibre engineered cementitious composite using Grey-Taguchi method and utility concept, *Construct. Build. Mater.* 319 (2022) 126040.
- [13] Z. Zhang, F. Yang, J.C. Liu, S. Wang, Eco-friendly high strength, high ductility engineered cementitious composites (ECC) with substitution of fly ash by rice husk ash, *Cement Concr. Res.* 137 (2020) 106200.
- [14] M. Hou, D. Zhang, V.C. Li, Material processing, microstructure, and composite properties of low carbon Engineered Cementitious Composites (ECC), *Cement Concr. Compos.* 134 (2022) 104790.
- [15] E. Aprianti, P. Shafiqh, R. Zawawi, Z.F.A. Hassan, Introducing an effective curing method for mortar containing high volume cementitious materials, *Construct. Build. Mater.* 107 (2016) 365–377.
- [16] A.A. Shubbar, H. Jafer, M. Abdulredha, Z.S. Al-Khafaji, M.S. Nasr, Z. Al Masoodi, M. Sadique, Properties of cement mortar incorporated high volume fraction of GGBFS and CKD from 1 day to 550 days, *J. Build. Eng.* 30 (2020) 101327.
- [17] M.A. Sherir, K.M. Hossain, M. Lachemi, Development and recovery of mechanical properties of self-healing cementitious composites with MgO expansive agent, *Construct. Build. Mater.* 148 (2017) 789–810.
- [18] H. Wu, J. Yu, Y. Du, V.C. Li, Mechanical performance of MgO-doped engineered cementitious composites (ECC), *Cement Concr. Compos.* 115 (2021) 103857.
- [19] H. Wu, D. Zhang, B.R. Ellis, V.C. Li, Mechanical behavior of carbonated MgO-based Engineered Cementitious Composite (ECC) after high temperatures exposure, *Cement Concr. Compos.* 124 (2021) 104255.
- [20] D. Zhang, H. Wu, V.C. Li, B.R. Ellis, Autogenous healing of Engineered Cementitious Composites (ECC) based on MgO-fly ash binary system activated by carbonation curing, *Construct. Build. Mater.* 238 (2020) 117672.
- [21] T. Gonçalves, R.V. Silva, J. De Brito, J.M. Fernández, A.R. Esquinas, Mechanical and durability performance of mortars with fine recycled concrete aggregates and reactive magnesium oxide as partial cement replacement, *Cement Concr. Compos.* 105 (2020) 103420.
- [22] J. Zhang, Recent advance of MgO expansive agent in cement and concrete, *J. Build. Eng.* 45 (2022) 103633.

- [23] H.L. Wu, D. Zhang, Y.J. Du, V.C. Li, Durability of engineered cementitious composite exposed to acid mine drainage, *Cement Concr. Compos.* 108 (2020) 103550.
- [24] M.A. Sherir, K.M. Hossain, M. Lachemi, Self-healing and expansion characteristics of cementitious composites with high volume fly ash and MgO-type expansive agent, *Construct. Build. Mater.* 127 (2016) 80–92.
- [25] S. Rawat, C.K. Lee, Y.X. Zhang, Performance of fibre-reinforced cementitious composites at elevated temperatures: a review, *Construct. Build. Mater.* 292 (2021) 123382.
- [26] J.C. Liu, K.H. Tan, Fire resistance of ultra-high performance strain hardening cementitious composite: residual mechanical properties and spalling resistance, *Cement Concr. Compos.* 89 (2018) 62–75.
- [27] S. Pourfalah, Behaviour of engineered cementitious composites and hybrid engineered cementitious composites at high temperatures, *Construct. Build. Mater.* 158 (2018) 921–937.
- [28] A.A. Deshpande, D. Kumar, R. Ranade, Influence of high temperatures on the residual mechanical properties of a hybrid fiber-reinforced strain-hardening cementitious composite, *Construct. Build. Mater.* 208 (2019) 283–295.
- [29] WB/T1019, Caustic Burned Magnesia for Magnesium Oxychloride Cement Products, Professional Standard of the People's Republic of China, State Commission for Economic and Trade, Beijing, China, 2002 (In Chinese).
- [30] F. Ahmad, S. Rawat, R. Yang, L. Zhang, Y. Guo, D. Fanna, Y.X. Zhang, Effect of hybrid fibres on mechanical behaviour of magnesium oxychloride cement-based composites, *Construct. Build. Mater.* 424 (2024) 135937.
- [31] S. Rawat, Y.X. Zhang, D.J. Fanna, C.K. Lee, Development of sustainable engineered cementitious composite with enhanced compressive performance at elevated temperatures using high volume GGBFS, *J. Clean. Prod.* 451 (2024) 142011.
- [32] M.H. Lai, Y.M. Xie, B.X. Zhang, F.M. Ren, S. Kitipornchai, J.C.M. Ho, Iron sand heavy-weight concrete–pre-and post-fire characteristics from wet packing density perspective, *Construct. Build. Mater.* 435 (2024) 136728.
- [33] M.H. Lai, Z.Y. Lu, Y.T. Luo, F.M. Ren, J. Cui, Z.R. Wu, J.C.M. Ho, Pre-and post-fire behaviour of glass concrete from wet packing density perspective, *J. Build. Eng.* 86 (2024) 108758.
- [34] Z.C. Huang, J.J. Liu, F.M. Ren, J. Cui, Z. Song, D.H. Lu, M.H. Lai, Behavior of SSFA high-strength concrete at ambient and after exposure to elevated temperatures, *Case Stud. Constr. Mater.* 20 (2024) e02946.
- [35] S. Rawat, P. Saliba, P.C. Estephan, F. Ahmad, Y. Zhang, Mechanical performance of hybrid fibre reinforced magnesium oxychloride cement-based composites at ambient and elevated temperature, *Buildings* 14 (1) (2024) 270.
- [36] J. Vongsvivut, D. Pérez-Guaita, B.R. Wood, P. Heraud, K. Khambatta, D. Hartnell, M.J. Hackett, M.J. Tobin, Synchrotron macro ATR-FTIR microspectroscopy for high-resolution chemical mapping of single cells, *Analyst* 144 (10) (2019) 3226–3238.
- [37] ACI Committee 363, High-Strength Concrete (ACI 363R), vol. 228, 2005, pp. 79–80.
- [38] J. Yu, J. Lin, Z. Zhang, V.C. Li, Mechanical performance of ECC with high-volume fly ash after sub-elevated temperatures, *Construct. Build. Mater.* 99 (2015) 82–89.
- [39] S. Rawat, C.K. Lee, Y.X. Zhang, Green engineered cementitious composites with enhanced tensile and flexural properties at elevated temperatures, *Clean. Mater.* 12 (2024) 100240.
- [40] X. Zhuang, Y. Liang, J.C.M. Ho, Y.H. Wang, M. Lai, X. Li, Z. Xu, Y. Xu, Post-fire behavior of steel slag fine aggregate concrete, *Struct. Concr.* 23 (6) (2022) 3672–3695.
- [41] J.C.M. Ho, Y. Liang, Y.H. Wang, M.H. Lai, Z.C. Huang, D. Yang, Q.L. Zhang, Residual properties of steel slag coarse aggregate concrete after exposure to elevated temperatures, *Construct. Build. Mater.* 316 (2022) 125751.
- [42] F. Jin, A. Al-Tabbaa, Strength and hydration products of reactive MgO–silica pastes, *Cement Concr. Compos.* 52 (2014) 27–33.